aerospace

MDPI

*Article*

# Experimental Investigation of Snow Cloud Evolution During Helicopter Operations over Snow-Covered Surfaces

**Tianshuang Shao [1,2], Wenkai Yu [1,*], Xiangnan Liu [1], Shi Liu [1], Zheng Yang [1] and Yuntong Li [1]**

[1] AVIC Aerodynamics Research Institute, Harbin 150001, China; shaots@avic.com (T.S.); liuxiangnan200851@163.com (X.L.); liushi_6060@163.com (S.L.); m18445865065@163.com (Z.Y.); yuntong98@163.com (Y.L.)
[2] Northwestern Polytechnical University, Xi'an 710072, China
* Correspondence: ywk666@163.com

**Abstract**

Helicopter operations over snow-covered surfaces are susceptible to whiteout conditions, which can severely degrade pilot visibility and threaten flight safety. To investigate the evolution characteristics and formation mechanisms of rotor-induced snow clouds during near-ground operations, a series of field experiments were conducted using an unmanned helicopter with a rotor diameter of 2.2 m under natural winter conditions. Image-processing techniques based on grayscale-difference analysis were employed to quantify snow cloud area and concentration, while planar laser qualitative flow visualization was used to examine snow particle motion and flow structures. The rotor-induced downwash is considered a dominant influencing factor affecting snow cloud formation and evolution under the present experimental conditions. During takeoff and landing, the proximity of the rotor to the ground strengthens the interaction between the downwash flow and the snow surface, resulting in enhanced snow particle entrainment and larger snow cloud areas. Increasing collective pitch tends to intensify the rotor-induced downwash, which may contribute to greater snow cloud extent and higher snow concentrations. The experiments also reveal that snow cloud evolution is characterized by a coupled process involving particle entrainment, suspension, recirculation, and deposition rather than simple transient dispersion. Flow visualization results indicate that rotor downwash initially generates a high-speed radial wall jet that mobilizes surface snow particles. Rotor tip vortices subsequently capture and transport these particles upward, promoting snow cloud growth and recirculation. The present study provides experimental insights into the physical mechanisms of helicopter-induced snow clouds and offers a basis for the assessment and mitigation of whiteout hazards during helicopter operations in snow-covered environments.

**Keywords:** helicopter; whiteout; snow cloud; rotor downwash; ground effect

Check for updates

Academic Editor: Konstantinos Kontis

Received: 27 June 2026
Revised: 12 August 2026
Accepted: 13 August 2026
Published: 28 August 2026

**Copyright:** © 2026 by the authors. Licensee MDPI, Basel, Switzerland. This article is an open access article distributed under the terms and conditions of the Creative Commons Attribution (CC BY) license.

## 1. Introduction

With the continuous development of rotorcraft technology, helicopters have been increasingly employed in a wide range of applications, including emergency rescue, environmental monitoring, and scientific exploration in remote and harsh environments. In particular, the growing demand for operations in snow-covered regions has made all-weather helicopter capability an important requirement for civilian missions. However, when a helicopter performs takeoff, landing, or near-ground hovering over a snow-covered surface, the rotor downwash can entrain large quantities of snow particles and generate

a recirculating snow cloud around the aircraft. This phenomenon, commonly referred to as whiteout, can rapidly obscure terrain features, horizon references, and visual cues required for safe flight operations, thereby increasing pilot workload and accident risk. Previous studies have shown that whiteout conditions can lead to a complete loss of visual references and severely degrade situational awareness during helicopter operations in snow-covered environments [1–3]. Therefore, understanding the formation, evolution, and operational impacts of rotor-induced snow clouds is of great importance for improving helicopter safety in cold-region operations.

The formation of rotor-induced particle clouds is fundamentally governed by the complex interaction between rotor wakes and the ground surface. Brown and Whitehouse [4] developed a numerical model to investigate rotor wake behavior in ground effect and demonstrated that the interaction between rotor downwash and the ground significantly modifies the wake structure, producing complex recirculation regions near the surface. To improve the prediction of rotor wake evolution, Brown and Line [5] proposed a high-resolution wake modeling approach based on the Vorticity Transport Model (VTM), which accurately captured the development of rotor vortices while maintaining computational efficiency. Building upon these studies, Lee et al. [6] investigated the interaction of blade-tip vortices with a ground plane and revealed the deformation, rebound, and redistribution of tip vortices in ground effect. Their findings provided further insight into the mechanisms governing near-ground rotor flow structures. Sydney and Leishman [7] experimentally examined rotor–airframe interactions over a sediment bed and showed that the rotor-induced flow field strongly influences the initiation of particle entrainment from the ground surface. Subsequently, Sydney and Leishman [8] conducted time-resolved measurements of rotor-induced particle flows generated by a hovering rotor and characterized the temporal evolution of particle transport within the wake flow field. Zhu et al. [9] employed CFD coupled with a hybrid trim algorithm to investigate the aerodynamic characteristics of helicopter rotors operating in ground effect, focusing on the variation in rotor-induced flow fields and aerodynamic performance with rotor height above the ground. Pasquali et al. [10] performed a coupled numerical–experimental investigation of hovering rotor aerodynamics in ground effect and demonstrated that near-ground recirculation plays an important role in modifying the induced flow field and rotor loading. These studies established an important foundation for understanding the aerodynamic mechanisms responsible for particle cloud formation during helicopter operations near the ground.

To investigate the transport and evolution of particulate clouds generated by rotorcraft, extensive efforts have been devoted to numerical simulations of the brownout phenomenon. Phillips and Brown [11] coupled an Eulerian particle transport model with rotor wake simulations to study the fluid dynamics of helicopter brownout. Their results demonstrated that the distribution of ground vortices and recirculating flow structures plays a dominant role in determining the shape and extent of dust clouds. Phillips et al. [12] further explored the flow physics of helicopter brownout and analyzed the mechanisms governing particle entrainment, transport, and recirculation within rotor-induced flow fields. Recognizing the importance of accurately modeling particle pickup processes, Jasion [13] developed a physics-based entrainment model for helicopter brownout simulations, providing improved predictions of sediment entrainment from the ground surface. Porcù et al. [14] employed high-performance computing techniques and a noninteracting particle dynamics model to perform large-scale brownout simulations, demonstrating the capability of advanced numerical methods to predict particle transport and cloud evolution. More recently, Cao et al. [15] adopted a CFD–DEM approach to investigate the factors influencing brownout development and analyzed the effects of operating and environmental

parameters on particle cloud evolution. These studies have significantly improved the understanding and predictive capability of brownout simulations.

Experimental investigations have played a crucial role in validating numerical models and improving the understanding of rotor-induced particle clouds. To quantitatively characterize brownout clouds, Tanner [16] applied photogrammetric techniques to obtain spatial information on dust cloud development. Wong and Tanner [17] subsequently performed photogrammetric measurements of an EH-60L brownout cloud and provided detailed three-dimensional cloud characteristics for model validation. Advanced optical diagnostics have also been introduced into rotorcraft flow research. Raffel et al. [18] reviewed the application of Particle Image Velocimetry (PIV) in helicopter aerodynamics and highlighted its potential for investigating complex rotor wake structures and rotor-environment interactions. Although brownout and whiteout are often discussed together because both involve rotor-induced particle clouds that degrade pilot visibility, their governing physical mechanisms differ substantially [19,20]. Brownout is dominated by dry sand or dust particles with relatively high density, weak inter-particle cohesion, and comparatively limited optical scattering. In contrast, snow particles generally possess lower density, irregular crystal morphology, temperature-dependent adhesion, and much stronger multiple-scattering characteristics under visible illumination. Consequently, snow particles are more susceptible to suspension, recirculation, aggregation, and optical attenuation, making the evolution of whiteout fundamentally different from that of brownout. Therefore, conclusions derived from brownout studies cannot be directly extended to snow-covered environments, highlighting the need for dedicated experimental investigations of helicopter whiteout.

Compared with brownout, experimental studies on helicopter whiteout remain very limited. One of the earliest investigations was conducted by Ebersole [21], who examined the influence of snow properties on whiteout severity during helicopter operations. However, due to the limitations of experimental techniques available at that time, the measurements mainly relied on visual observations and pilot evaluations, providing limited quantitative information on snow cloud evolution, particle concentration distribution, and flow-field development. Consequently, the transient evolution mechanisms of rotor-induced snow clouds remain insufficiently understood. In addition, Zhou et al. [22] developed a two-equation model for the numerical simulation of wind-blown snow and investigated the transport and redistribution of snow particles driven by airflow. Matsuzawa and Takeuchi [23] investigated methods for estimating visibility under blowing snow conditions and established relationships between snow particle concentration and visual range. Ryerson et al. [24] studied visibility enhancement technologies for rotorwash-induced particle clouds and evaluated sensing approaches aimed at improving pilot situational awareness in degraded visual environments.

Beyond cloud characterization, increasing attention has been devoted to degraded visual environment (DVE) mitigation and visibility assessment. The NATO report on rotary-wing brownout mitigation [25] summarized available technologies and training strategies for reducing brownout-related operational risks. Viertler and Hajek [26] evaluated visual augmentation methods for rotorcraft pilots and demonstrated their effectiveness in improving situational awareness under reduced-visibility conditions. Montalban [27] further investigated LiDAR-based perception technologies and proposed a probabilistic framework for visibility estimation in degraded visual environments. For snow-covered environments, the optical characteristics of snow particles are also of critical importance. Warren [28] comprehensively reviewed the optical properties of snow and ice and demonstrated that snow exhibits strong scattering and reflection characteristics in the visible spectrum. These optical properties can substantially influence visibility degradation mechanisms and distinguish helicopter whiteout from the conventional brownout phenomenon.

Although significant progress has been achieved in rotor wake modeling, brownout simulations, and visibility assessment, most existing studies have focused on dust-induced brownout phenomena. Experimental investigations of rotor-induced snow cloud evolution under realistic snow-covered conditions remain relatively limited. Unlike previous studies focusing primarily on rotor aerodynamics, brownout, or qualitative observations of whiteout, the present study aims to quantitatively investigate the temporal and spatial evolution of rotor-induced snow clouds during helicopter takeoff, landing, and near-ground hovering. In particular, the coupling among rotor operating conditions, near-ground flow, snow-particle entrainment, and snow cloud development has not been sufficiently characterized experimentally. Field experiments were conducted using a 2.2 m rotor-diameter unmanned helicopter under natural winter conditions in Harbin, China. The experimental setup, measurement system, and test procedures are first presented. Representative takeoff, landing, and hovering cases are then analyzed to reveal the temporal and spatial evolution of the snow cloud. Furthermore, laser-sheet qualitative flow visualization measurements are performed to examine the snow particle motion and entrainment processes within the rotor-induced flow field. The findings contribute to a better understanding of the helicopter whiteout phenomenon and provide experimental data for the validation and development of numerical prediction models.

## 2. Experimental Setup

### *2.1. Helicopter Model*

An unmanned helicopter with a single main rotor and two-blade configuration was used as the experimental model. As shown in Figure 1, the rotor diameter was 2.2 m, and the blade chord was 72 mm. The rotor hub height above ground was 0.64 m, and the rotor rotated clockwise when viewed from above. The main geometric characteristics of the helicopter are summarized in Table 1.




(**a**)



(**b**)

**Figure 1.** Unmanned helicopter used in the experiments: (**a**) overall view; (**b**) rotor blade.

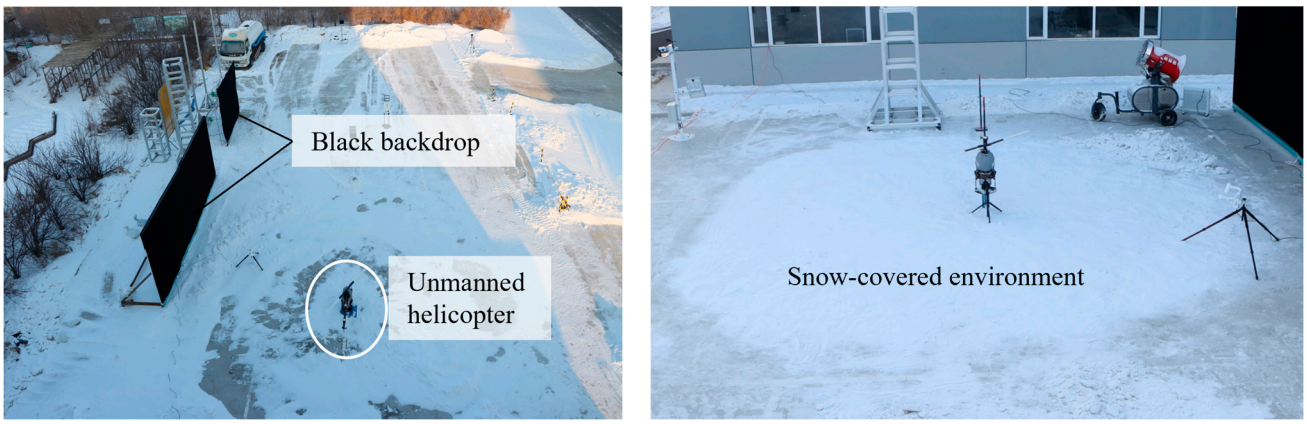
The helicopter was equipped with a ground control station capable of real-time acquisition, transmission, and recording of flight data. Key operating parameters, including rotor speed and collective pitch, were continuously monitored throughout the experiments to ensure accurate test condition control and support subsequent data analysis.

**Table 1.** Main parameters of the unmanned helicopter.

| Parameter | Value |
|---|---|
| Number of rotor blades | 2 |
| Rotor diameter (m) | 2.2 |
| Maximum takeoff weight (kg) | 48 |
| Fuselage length (m) | 2.6 |
| Rotor height above ground (m) | 0.64 |
| Rotor rated speed (r·min$^{-1}$) | 1210 |

### 2.2. Test Site

The experiments were conducted at an outdoor test site in Harbin during winter, as shown in Figure 2. Naturally fallen snow was collected from the surrounding area and uniformly spread over the test surface. Centered on the ground projection of the rotor hub, a circular snow-covered area with a diameter of 10 m was prepared. A snow layer approximately 3 cm thick was maintained to simulate helicopter operations over snow-covered surfaces and to ensure sufficient snow availability for the development of rotor-induced snow clouds. The experiments were conducted under relatively calm environmental conditions, with the ambient wind speed maintained below 1 m/s. Wind direction, gust speed, and relative humidity were not continuously monitored during the experiments. Therefore, the effects of these environmental parameters were not quantitatively evaluated in the present study. The snow used for the experiments was fresh snow that had fallen within approximately 24 h before testing. The average snow density was approximately 0.3 g/cm$^3$. Before each test, the snow was manually distributed over the designated test area to obtain a relatively uniform initial snow-covered surface. However, the snow grain size and the spatial uniformity of the snow layer were not quantitatively characterized.




(**a**) (**b**)

**Figure 2.** Test site and simulated snow-covered environment: (**a**) test site; (**b**) simulated snow-covered environment.

### 2.3. Hovering Support System

To ensure stable hovering and reliable data acquisition during the experiments, a dedicated hovering support system was developed for the unmanned helicopter, as shown in Figure 3. The system incorporated a spherical hinge mechanism to facilitate attitude adjustment and alignment. During the hovering tests, the helicopter was securely attached to the support structure through a connecting plate. The adjustment rods were then fine-tuned to position the helicopter in the prescribed hovering attitude.

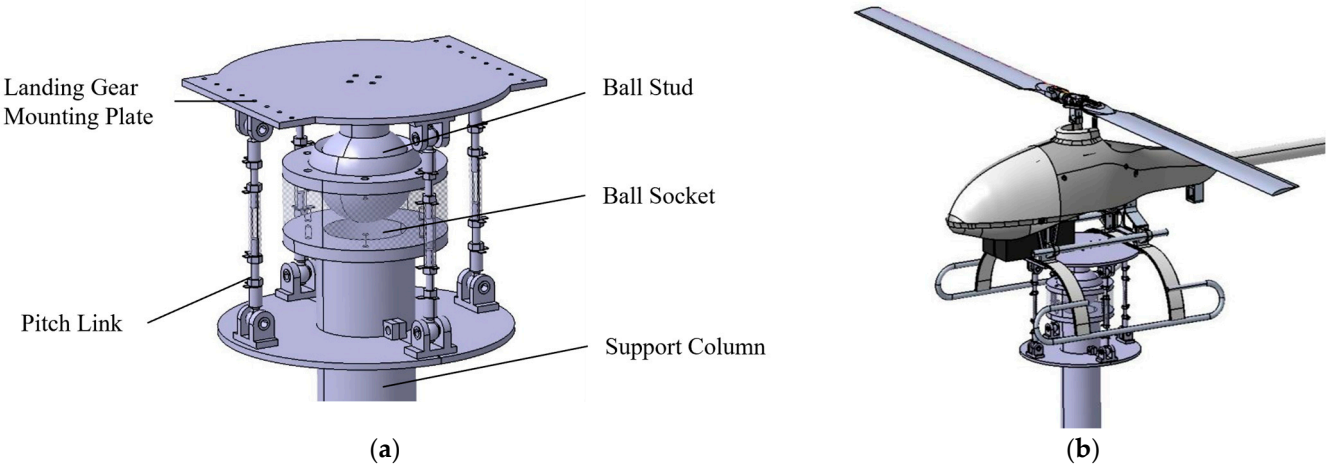



**Figure 3.** Hovering support system for the unmanned helicopter: (**a**) support system; (**b**) helicopter installation.

## 3. Experimental Methods

### *3.1. Force Analysis of Snow Particles*

During helicopter flight, a strong rotor-induced downwash is generated beneath the rotor. When the helicopter is taking off, landing, or hovering close to the ground, the interaction between the rotor downwash and the ground produces a pronounced ground-effect flow field. After impinging on the ground, the high-speed downwash spreads radially outward, forming a radial wall jet in the near-ground region. As the flow develops outward, the wall-jet velocity gradually decreases, and a recirculation structure is established in the outer region. Part of the airflow moves upward and is subsequently re-entrained into the rotor-induced flow, resulting in a large-scale recirculating flow pattern [29].

Over snow-covered surfaces, the rotor-induced flow field not only modifies the near-ground airflow structure but also provides the aerodynamic forcing required for snow particle entrainment. Under the action of the rotor-induced flow, snow particles must overcome gravitational and surface constraint forces to transition from a stationary state to motion. For an individual snow particle resting on the snow surface, the primary forces include gravity, drag force, lift force, and friction force, as illustrated in Figure 4.

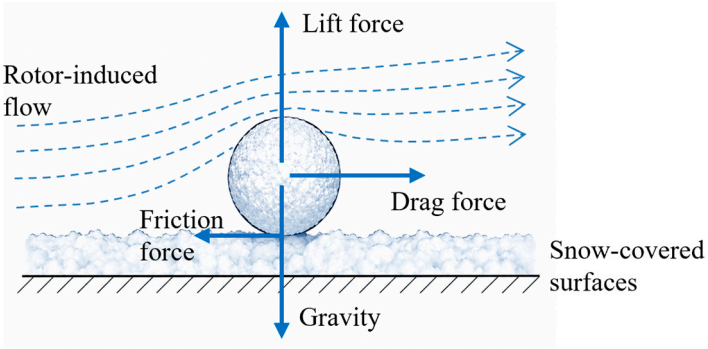



**Figure 4.** Schematic diagram of the forces acting on a snow particle.

As the rotor speed and collective pitch increase, the downwash velocity continuously rises, leading to corresponding increases in the drag and lift forces acting on the snow particles. Once the aerodynamic forces exceed the combined effects of gravity and frictional resistance, snow particles become detached from the snow surface and are entrained into the airflow. Some of the entrained particles are transported upward by the recirculating

flow and subsequently accumulate within the rotor-induced flow field, forming high-concentration snow clouds.

### *3.2. Measurement Method for Snow Cloud Evolution*

To investigate the formation and evolution of snow clouds induced by rotor downwash, an image-based measurement method was developed for near-ground helicopter operations over snow-covered surfaces. The method utilizes the scattering characteristics of snow particles under visible-light illumination. Changes in image grayscale values reflect variations in the intensity of scattered light and were therefore used to characterize the spatiotemporal evolution of snow clouds [30,31]. Accordingly, grayscale difference was selected as the primary parameter for quantitative analysis.

#### 3.2.1. Snow Cloud Image Acquisition

A Canon EOS 90D camera (Canon Inc., Tokyo, Japan) was used to acquire image sequences of the experiments at a frame rate of 25 fps. The experimental setup is shown in Figure 5. The camera was positioned laterally relative to the unmanned helicopter to capture the complete spatial diffusion pattern of the whiteout cloud. Three black backdrops, each measuring 4 m × 3 m, were installed within the camera field of view to enhance the contrast between the snow cloud and the background. This arrangement minimized the effects of ambient lighting variations and background textures, thereby improving the accuracy and robustness of snow cloud identification and feature extraction.

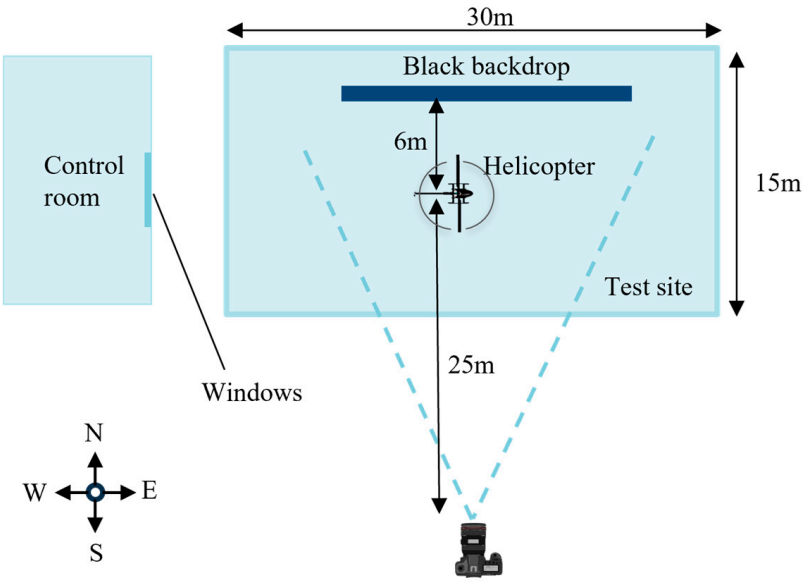



**Figure 5.** Experimental setup for snow cloud measurements.

#### 3.2.2. Snow Cloud Region Identification

Because the background remained nearly unchanged during the experiments—whereas snow particle entrainment and transport produced significant temporal variations in image grayscale values—a background-subtraction-based grayscale-difference threshold method was adopted for snow cloud identification. Compared with direct grayscale threshold segmentation, this method effectively removes interference from static background features, including bright objects and non-uniform illumination, and enhances the contrast of snow cloud regions, thereby improving identification accuracy. It should be noted that illumination variability is a potential source of uncertainty for grayscale-difference-based snow cloud identification. In the present experiments, the image sequences used for quantitative analysis were acquired under relatively stable illumination conditions, and

no substantial illumination changes were observed within each measurement sequence. Therefore, illumination-induced variations were considered to have a limited influence on the extracted snow cloud boundaries under the present experimental conditions.

The original images were first converted into grayscale images. Twenty frames captured before the onset of snow cloud formation were selected, and their average grayscale image was calculated as the static background reference:

$$I_{bg}(x,y) = \frac{1}{N}\sum_{k=1}^{N} I_k(x,y),\ N = 20 \tag{1}$$

where $I_k(x,y)$ is the grayscale value of the snow-free background image, and $(x,y)$ denotes the image coordinates.

During the test, let $I(x,y)$ denote the grayscale value of the image at time $t$. The grayscale difference relative to the background reference is calculated as:

$$D(x,y) = I(x,y) - I_{bg}(x,y) \tag{2}$$

A binary segmentation procedure was then performed using a grayscale-difference threshold $T$:

$$B(x,y) = \begin{cases} 1, & D(x,y) > T \\ 0, & D(x,y) \le T \end{cases} \tag{3}$$

To determine an appropriate threshold for snow cloud segmentation, a sensitivity assessment was performed using different grayscale-difference thresholds. When ($T < 12$), uneven illumination and background textures produced a relatively large number of false-positive regions, particularly in areas with weak snow-cloud signals. In contrast, when ($T > 18$), portions of the sparse snow cloud were not detected, resulting in an incomplete representation of the cloud boundary. Through comparative evaluation, a threshold value of $T = 15$ was found to provide a favorable balance between identification completeness and background noise suppression. Therefore, $T = 15$ was selected as the optimal threshold for snow cloud segmentation. Pixels whose grayscale difference exceeded 15 were identified as belonging to the snow cloud region and were marked in red for visualization. Examples of the original images and the corresponding snow cloud identification results are presented in Figure 6.

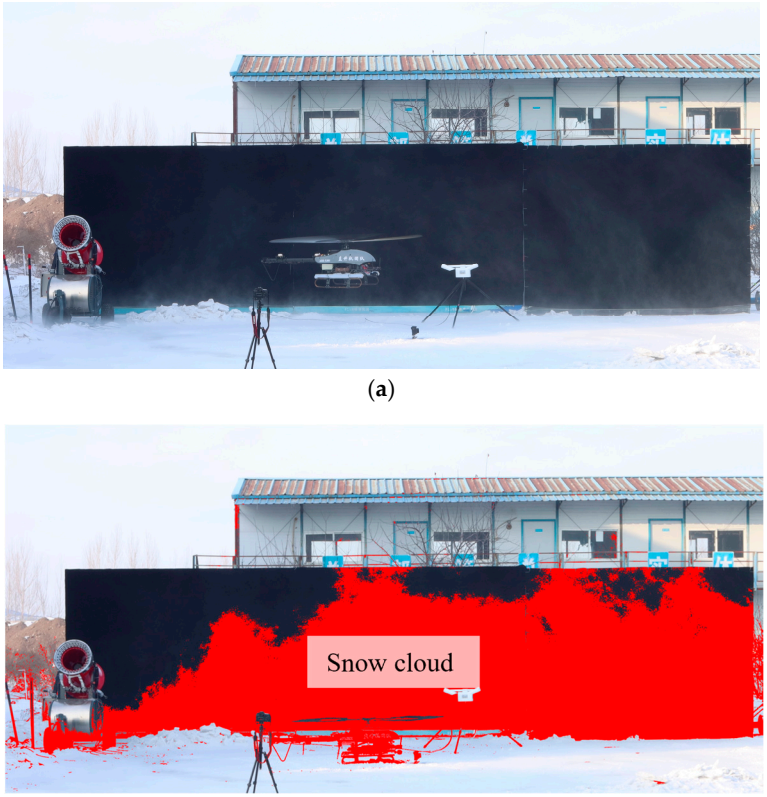
To further characterize the geometric features of the snow cloud, post-processing was applied to the binary images. Morphological closing operations, image dilation, and Gaussian filtering were used to suppress random noise [32,33]. Subsequently, the Canny edge detection algorithm was employed to extract the snow cloud boundary [34].

To convert image coordinates into physical dimensions, a scale factor was established using the known physical diameter of the rotor and its corresponding pixel diameter in the image. However, no perspective correction was applied during the image processing. The actual snow cloud area $A$ and horizontal spreading distance $L$ were obtained:

$$A = k \cdot \sum_{x,y} B(x,y) \tag{4}$$

$$L = k \cdot ax\left(x'_i\right) \tag{5}$$

where $\{(x'_i, y'_i)\}$ denotes the set of boundary contour points, and $k$ is the conversion coefficient between the physical dimensions and image pixels.




(**a**)

(**b**)

**Figure 6.** Example of snow cloud identification: (**a**) original image; (**b**) identified snow cloud region.

#### 3.2.3. Relative Snow Cloud Concentration Indicator

A typical sequence of snow cloud evolution images captured during the experiments is shown in Figure 7, where $t$ = 0 s denotes the onset of rotor startup. The image sequence illustrates the evolution of the snow cloud from its initial formation to its subsequent development in the vicinity of the rotor.

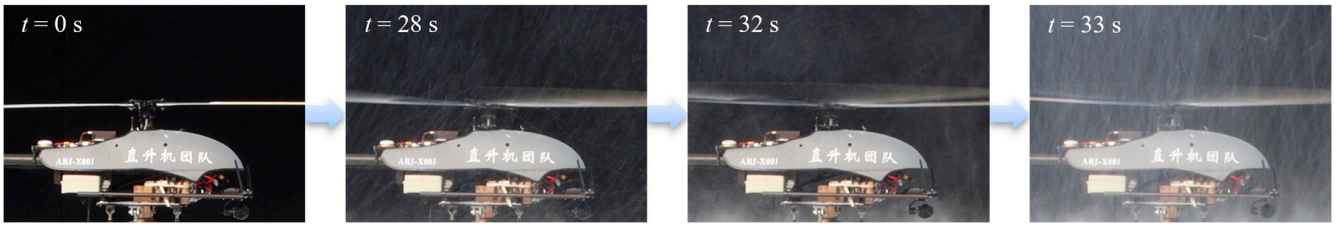



**Figure 7.** Typical snow cloud evolution sequence (rotor speed: 1210 r·min$^{-1}$; collective pitch: 7.65°; rotor height/radius: 1).

While the snow cloud identification procedure provides information regarding the macroscopic geometric evolution of the snow cloud, additional quantitative analysis is required to characterize its internal structure. Therefore, several regions of interest (ROIs) with dimensions of 0.2 m × 0.2 m were selected at different locations within the primary snow cloud spreading region.

For the ROI$i$ at time $t$, the mean grayscale value is denoted by $I_{ROIi}$. The corresponding background grayscale value measured during the snow-free stage is denoted by $I_{ROIi}^{bg}$. The grayscale difference in the ROI$i$ is defined as:

$$D_{ROIi} = I_{ROIi} - I_{ROIi}^{bg}, i = 1, 2 \cdots, 6 \quad (6)$$

This grayscale-difference metric reflects the variation in snow cloud concentration at different spatial locations during snow particle entrainment and transport. Larger grayscale differences indicate higher snow particle concentrations and denser snow cloud regions, whereas smaller values correspond to lower concentrations and more dispersed snow clouds. In this study, the grayscale difference is used only as a relative indicator of the spatial and temporal variation in snow cloud density. It is not directly converted into an absolute snow particle mass concentration because an independent calibration between grayscale difference and snow mass concentration was not established.

### *3.3. Test Conditions and Experimental Procedures*

The experiments were conducted under ambient temperatures consistently below −7 °C to prevent melting and agglomeration of the surface snow. Snow cloud evolution measurements were first performed under two operating conditions, namely takeoff and landing and fixed-height hovering. These tests were conducted during daytime under natural illumination to capture the macroscopic morphology and spatial evolution of the snow cloud. Subsequently, planar laser qualitative flow visualization experiments were carried out under hovering conditions to investigate the flow structures and snow particle entrainment mechanisms induced by rotor downwash. To enhance laser illumination and image quality, these experiments were performed at night under low ambient light conditions.

The operating conditions for the takeoff and landing test and hovering tests are summarized in Tables 2 and 3, respectively. The rotor speed was selected as the rated operating speed of the unmanned helicopter. The collective pitch angles were selected according to practical operating conditions corresponding to different loading states. The rotor height was selected as 1R above the ground, corresponding to a typical low-altitude hovering condition. Due to the dependence of the experiment on loose fresh snow conditions, repeated tests under exactly identical snow conditions were limited. Although statistical repeatability could not be evaluated through multiple repetitions, the experiments were conducted under controlled rotor operating conditions and consistent snow preparation procedures. Therefore, the obtained results mainly represent the physical evolution characteristics of rotor-induced snow clouds under typical near-ground operating conditions.

**Table 2.** Test conditions for takeoff and landing experiments.

| Test No. | Rotor Speed (r·min$^{-1}$) | Collective Pitch (°) | Takeoff Weight (kg) | Climb Height (m) |
|---|---|---|---|---|
| T01 | 1210 | 7.65 | 38.66 | 8.8 |

**Table 3.** Test conditions for hovering experiments.

| Test No. | Rotor Speed (r·min$^{-1}$) | Collective Pitch (°) | Rotor Height/Radius |
|---|---|---|---|
| T02 | 1210 | 6.00 | 1 |
| T03 | 1210 | 7.65 | 1 |
| T04 | 1210 | 7.65 | 1 |

Taking the snow cloud evolution measurement experiment as an example, the experimental procedure is described as follows:

(a) Black backdrops were installed at the test site.
(b) The camera was positioned outside the expected snow cloud region on the lateral side of the helicopter.
(c) The tests were conducted according to the prescribed operating conditions. For the takeoff-and-landing tests, the unmanned helicopter was placed at the designated location within the test area. For the fixed-height hovering tests, the support system

was first adjusted to the prescribed height and locked in place. The helicopter was then mounted on the support system, and its attitude was adjusted to the desired hovering condition using an inclinometer.

(d) Snow was collected and uniformly distributed over the test area to simulate a snow-covered operating environment.

(e) Image acquisition was initiated using the camera system.

(f) The rotor speed was first increased to 100 r·min$^{-1}$ for warm-up. Meanwhile, communication between the unmanned helicopter and the ground control station was verified to ensure normal operation of the control, data transmission, and measurement systems.

(g) During the takeoff-and-landing tests, the throttle input was gradually increased to start the helicopter and increase the collective pitch, allowing the helicopter to complete the takeoff, hover, and landing sequence.

(h) During the hovering tests, the rotor speed, collective pitch, or thrust was adjusted to the prescribed value. The helicopter was brought to a stable operating condition as quickly as possible and maintained at this condition throughout the test. The helicopter was shut down after the airborne snow particle concentration had significantly decreased and the snow cloud had dissipated.

## 4. Results and Discussion

### *4.1. Snow Cloud Evolution During Takeoff and Landing*

The T01 takeoff and landing experiment was conducted to investigate the formation and evolution of snow clouds during helicopter operations over snow-covered surfaces. The corresponding test conditions are summarized in Table 2. The timeline of helicopter operating states and snow cloud evolution is summarized in Table 4, while the variation in helicopter flight height $h$ during the experiment is presented in Figure 8.

**Table 4.** Timeline of helicopter operating states and snow cloud evolution during the T01 experiment.

| No. | Description | Time, $t$ (s) |
|---|---|---|
| 1 | Helicopter start-up | 0 |
| 2 | Onset of snow cloud formation | 24 |
| 3 | Lift-off | 26 |
| 4 | Peak snow cloud during climb | 37.2 |
| 5 | Maximum height reached (8.8 m) | 46 |
| 6 | Minimum snow cloud area | 53.4 |
| 7 | Peak snow cloud during descent | 77 |
| 8 | Touchdown | 78 |
| 9 | Snow cloud dissipation completed | 86 |

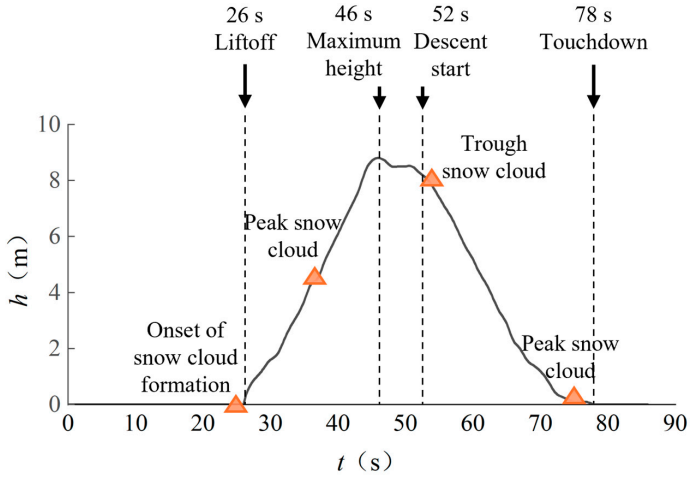



**Figure 8.** Variation in helicopter flight height during the T01 experiment.

Image sequences capturing the helicopter motion and snow cloud evolution during the period from $t$ = 24 s to 86 s are presented in Figure 9.

To quantitatively characterize snow cloud evolution, the snow cloud area was extracted from the captured images. To eliminate interference from the ground, sky, and other irrelevant regions, only the region covered by the black backdrop was retained for image processing. Accordingly, the snow cloud area during the T01 experiment, denoted as $A_v$, is defined as the snow cloud area within the background curtain region. Based on the image processing results, the temporal variations in the snow cloud area $A_v$ and helicopter flight altitude are shown in Figure 10.

As shown in Figure 10, the snow cloud area exhibits a characteristic "increase–decrease–increase–decrease" pattern correlated with variations in helicopter altitude. At $t$ = 24 s, snow particles beneath and around the rotor were entrained by the rotor downwash, marking the onset of snow cloud formation. The snow cloud subsequently expanded upward and outward. By $t$ = 26 s, when the helicopter lifted off, the snow cloud had already covered a substantial portion of the background region. During the period from $t$ = 28.2 s to 32.6 s, the snow cloud area temporarily decreased from 14.4 $m^2$ to 12.0 $m^2$ before increasing again. Meteorological measurements at the test site indicate that this fluctuation was induced by an intermittent gust, which temporarily enhanced snow cloud dispersion. The snow cloud area reached its first peak of 20.6 $m^2$ at $t$ = 37.2 s, when the helicopter altitude was approximately 4.6 m and still increasing. As the helicopter continued to ascend, the influence of rotor downwash on the snow surface gradually weakened, leading to a dissipation stage. Accordingly, the snow cloud area $A_v$ decreased significantly after $t$ = 42.8 s. At the maximum altitude ($t$ = 46 s), approximately half of the peak snow cloud area had dissipated, and the helicopter maintained a high-altitude hover until further decay of the cloud. As the rotor approached the ground, the interaction between the downwash flow and the snow surface intensified again, leading to renewed snow particle entrainment. Consequently, the snow cloud area increased and reached a second peak of 20.6 $m^2$ at $t$ = 77 s. After touchdown, the snow cloud gradually dissipated until the end of the experiment.

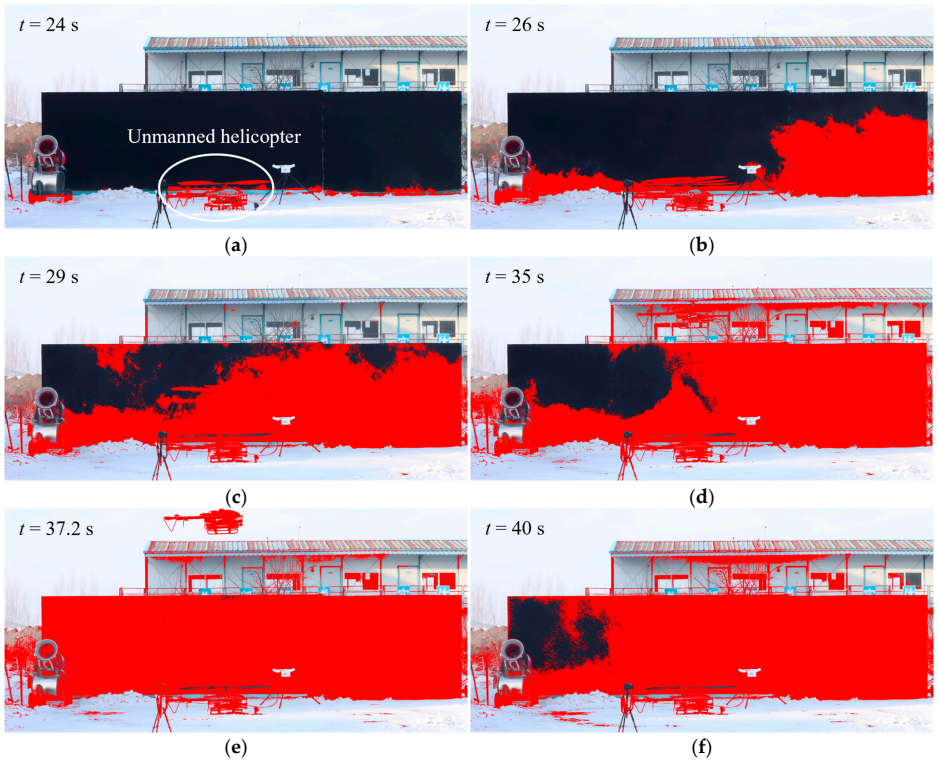



**Figure 9.** *Cont.*




**Figure 9.** Image sequence showing snow cloud formation and evolution during helicopter takeoff and landing: (**a**) $t$ = 24 s; (**b**) $t$ = 26 s; (**c**) $t$ = 29 s; (**d**) $t$ = 35 s; (**e**) $t$ = 37.2 s; (**f**) $t$ = 40 s; (**g**) $t$ = 46 s; (**h**) $t$ = 49 s; (**i**) $t$ = 53.4 s; (**j**) $t$ = 60 s; (**k**) $t$ = 66 s; (**l**) $t$ = 70 s; (**m**) $t$ = 77 s; (**n**) $t$ = 83 s.

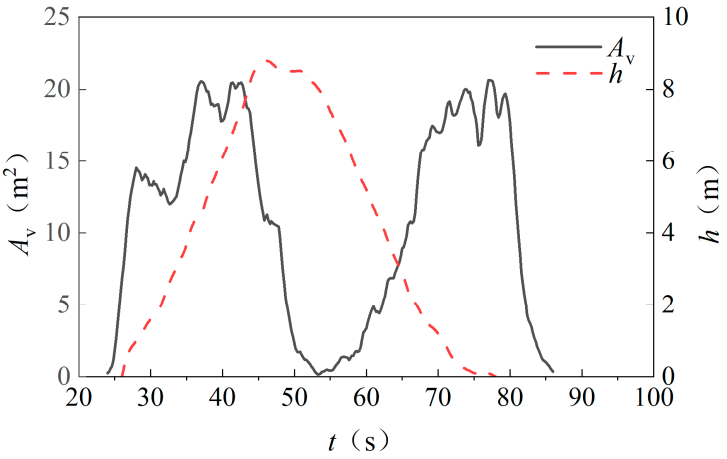



**Figure 10.** Temporal variations in snow cloud area and helicopter flight height during the T01 experiment.

Overall, the evolution of the snow cloud is strongly governed by helicopter altitude and rotor downwash intensity. During takeoff and landing phases, the proximity of the rotor to the ground enhances downwash-induced snow entrainment, resulting in larger snow cloud areas. In contrast, during high-altitude hovering, the reduced interaction between downwash flow and the snow surface leads to gradual dissipation. In addition,

external environmental disturbances, such as gusty winds, also play a non-negligible role in snow cloud dispersion. However, the tests were conducted under relatively stable low-temperature conditions, and the measurement region of interest was mainly within approximately 5 m from the rotor axis, where the snow cloud evolution was dominated by the rotor-induced flow field. Therefore, the influence of ambient wind fluctuations on the near-field snow cloud development was considered relatively limited.

### *4.2. Snow Cloud Evolution During Hovering*

The unmanned helicopter was mounted on the support device, and hovering experiments over snow-covered surfaces were conducted for Tests T02 and T03. The collective pitch angles were set to 6° and 7.65°, respectively, to investigate the formation and evolution characteristics of snow clouds during near-ground hovering under different collective pitch settings.

Since the onset of snow particle entrainment occurred at different times in the two tests, the instant at which snow particle entrainment was first observed was defined as $t' = 0$ s for each test to facilitate comparison. The timeline of rotor states and snow cloud evolution for Tests T02 and T03 is summarized in Table 5.

**Table 5.** Timeline of rotor operating states and snow cloud evolution during hovering experiments.

| No. | Description | $t'$-T02 (s) | $t'$-T03 (s) |
|---|---|---|---|
| 1 | Initial snow cloud formation | 0 | 0 |
| 2 | Rotor reaches test condition | 6.8 | 5.6 |
| 3 | Peak snow cloud development | 13.4 | 21 |
| 4 | Rotor deceleration begins | 35.8 | 25.6 |
| 5 | Snow cloud dissipation completed | 44 | 28.8 |

Image records corresponding to the representative stages of snow cloud evolution during Tests T02 and T03 are presented in Figure 11.

To quantitatively characterize snow cloud evolution, the snow cloud area and horizontal spreading distance were extracted from the recorded image sequence. To exclude interference from the ground surface, the lower portion of each image was removed prior to processing. In addition, because the dimensions of the black backdrop were insufficient to cover the entire test area, the curtain was positioned primarily on the right side of the rotor axis to ensure measurement accuracy within the main observation region. Consequently, only the region on the right side of the rotor axis was included in the analysis.

The snow cloud area and horizontal spreading distance were obtained using the snow cloud identification and boundary contour detection algorithms described previously. Based on the assumption that the snow cloud distribution was approximately symmetric about the rotor axis, the measured snow cloud area on the right side was multiplied by two to estimate the total snow cloud area, denoted as $A_{\mathrm{h}}$. This approximation is supported by the predominantly axisymmetric rotor-induced flow under the relatively calm experimental conditions. However, local asymmetry may result from ambient wind, non-uniform snow distribution, uneven snow entrainment, and imaging-background limitations. Therefore, the extrapolated cloud area should be regarded as an approximate estimate of the overall snow cloud extent rather than an exact reconstruction.

The temporal variations in the snow cloud area $A_{\mathrm{h}}$ and horizontal spreading distance $L$ are shown in Figure 12.

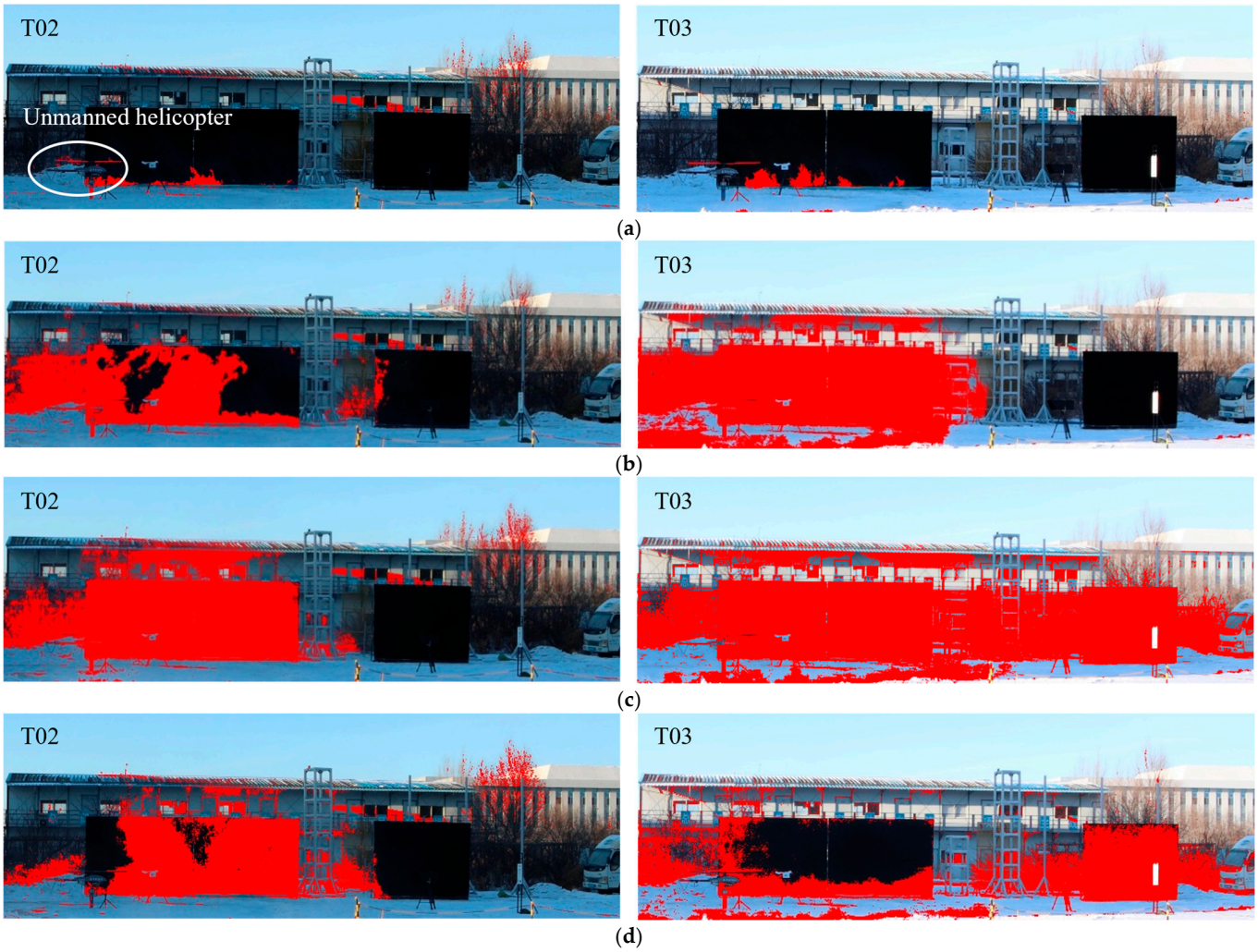



**Figure 11.** Representative stages of snow cloud evolution during Tests T02 and T03: (**a**) onset of snow cloud formation; (**b**) helicopter reaches the prescribed operating condition; (**c**) maximum snow cloud development; (**d**) initiation of rotor deceleration.

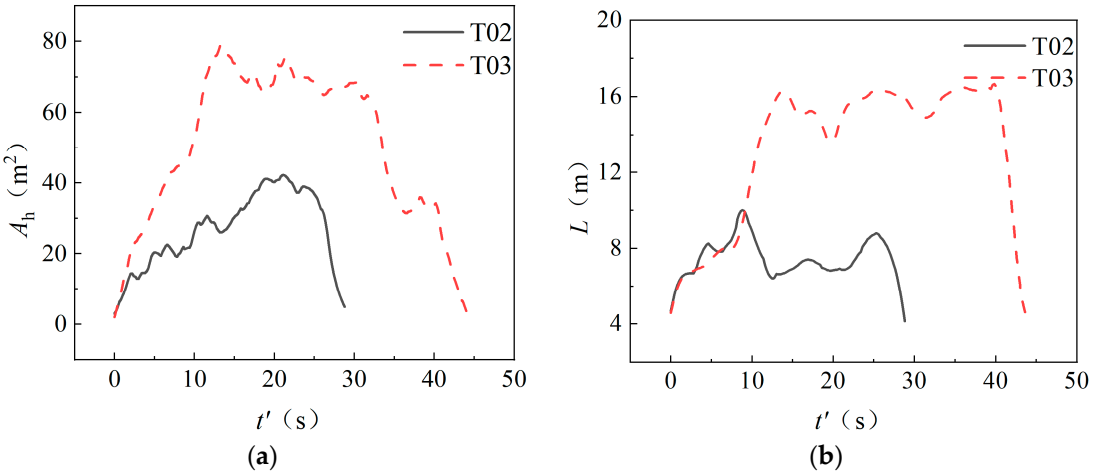



**Figure 12.** Temporal variations in snow cloud area and horizontal spreading distance under different collective pitch conditions: (**a**) snow cloud area; (**b**) horizontal spreading distance.

As shown in Figures 11 and 12, increasing the collective pitch resulted in a corresponding increase in rotor downwash velocity. Snow particles beneath and around the rotor were progressively entrained into the rotor downwash, marking the onset of snow

cloud formation. The snow cloud subsequently expanded upward and outward from its initial location. At $t'$ = 6.8 s, the snow cloud area in Test T03 reached 42.1 $m^2$, and the horizontal spreading distance extended to approximately 8 m from the rotor center. At the same time, the snow cloud area in Test T02 reached 22.1 $m^2$, while the horizontal spreading distance also extended to approximately 8 m. Continuous rotor downwash entrained snow particles from the surface and recirculated previously suspended particles above the rotor disk, generating a recirculating flow structure. Although some particles were transported beyond the observation region, continuous entrainment and recirculation maintained the overall snow cloud morphology for an extended period. The evolution of the snow cloud boundary further indicates that the rotor-induced flow continuously transported snow particles toward more distant regions. As the snow cover on the test surface was progressively redistributed by the rotor flow, snow near the rotor was gradually removed and transported outward. Snow particles deposited in distant regions eventually settled under the influence of gravity, leading to a gradual reduction in airborne particle concentration. After rotor shutdown, the snow cloud completely dissipated, marking the end of the experiment.

During the initial development stage ($t'$ = 0–9 s), the horizontal spreading distances in the two tests exhibited similar growth trends, and the difference in spreading distance remained relatively small. However, the snow cloud area in Test T03 was nearly twice that in Test T02, indicating that under the lower collective pitch setting in Test T02, snow particles remained concentrated near the ground and relatively few particles were transported to higher elevations. After $t'$ = 9 s, the snow cloud area continued to increase in both tests. However, the horizontal spreading distance in Test T02 exhibited a brief contraction before stabilizing, whereas that in Test T03 continued to expand rapidly before gradually reaching a quasi-steady state. During the period of stable rotor operation, both the snow cloud area and horizontal spreading distance remained relatively constant in each test. These results demonstrate that increasing collective pitch significantly enhances both the spatial extent and persistence of rotor-induced snow clouds by strengthening rotor downwash and promoting snow particle entrainment.

### *4.3. Snow Cloud Concentration Distribution During Hovering*

Based on the previously extracted snow cloud regions, six local regions of interest (ROIs), each measuring 0.2 m × 0.2 m, were selected within the primary snow cloud spreading region and denoted as ROI1–ROI6. As shown in Figure 13, a two-dimensional Cartesian coordinate system was established with the lower-left corner of the black backdrop defined as the origin. The *X*-axis extends horizontally to the right, whereas the *Y*-axis extends vertically upward. The rotor center was located at (0, 1.14 m). The coordinates of ROI1–ROI6 are listed in Table 6.

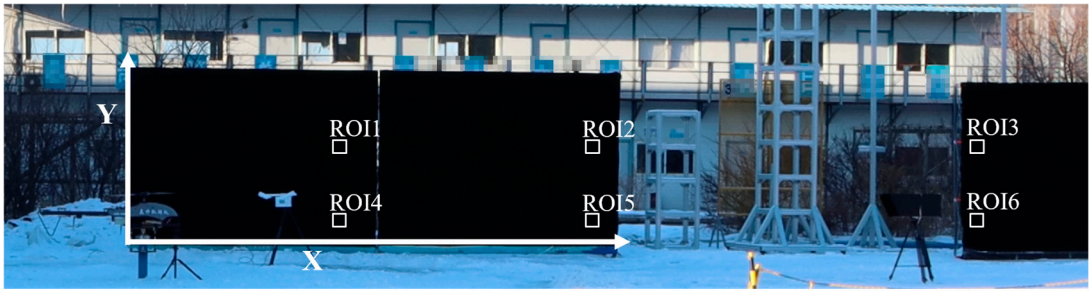



**Figure 13.** Locations of ROI1–ROI6.

**Table 6.** Coordinates of ROI1–ROI6.

| Region | X (m) | Y (m) |
|---|---|---|
| ROI1 | 2.8 | 1.5 |
| ROI2 | 6 | 1.5 |
| ROI3 | 11.3 | 1.5 |
| ROI4 | 2.8 | 0.3 |
| ROI5 | 6 | 0.3 |
| ROI6 | 11.3 | 0.3 |

The temporal variations in grayscale difference for ROI1–ROI6 in Tests T02 and T03 are shown in Figure 14, while the average grayscale differences during the snow entrainment stage are presented in Figure 15.

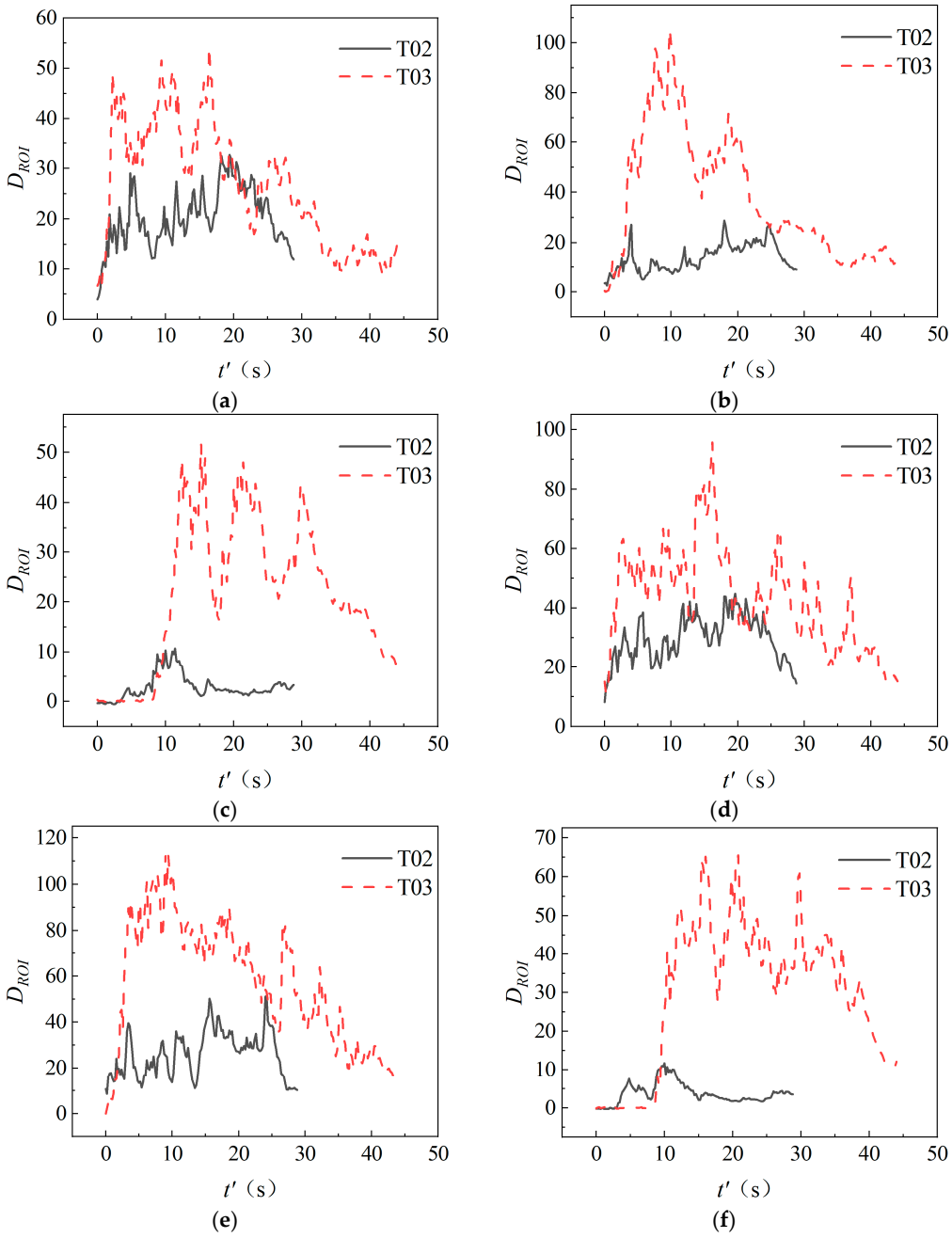



**Figure 14.** Temporal variations in grayscale difference in ROI1–ROI6 under different collective pitch conditions: (**a**) ROI1; (**b**) ROI2; (**c**) ROI3; (**d**) ROI4; (**e**) ROI5; (**f**) ROI6.

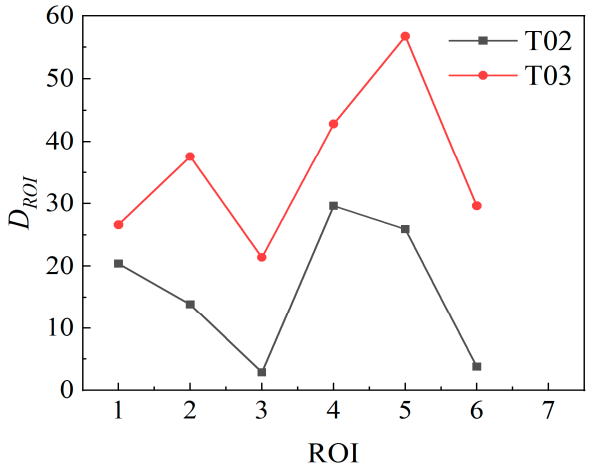



**Figure 15.** Average grayscale differences in ROI1–ROI6 under different collective pitch conditions.

As shown in Figures 14 and 15, the grayscale differences $D_{ROI4}$, $D_{ROI5}$, $D_{ROI6}$ measured at a height of 0.3 m are generally greater than $D_{ROI1}$, $D_{ROI2}$, $D_{ROI3}$ at 1.5 m, indicating that the snow cloud concentration below the rotor disk is higher than that above the rotor disk. The higher snow concentration observed at 0.3 m compared with that at 1.5 m height can be attributed to the characteristics of the rotor downwash and near-ground flow development. The rotor downwash impinges on the ground and generates a radial ground jet, which is the main mechanism responsible for transporting and redistributing entrained snow particles. The lower measurement height is closer to this high-momentum near-ground transport region, where snow particles experience stronger aerodynamic forcing and shorter transport distances from the entrainment source. With increasing height, particle concentration decreases due to vertical dispersion, particle settling, and dilution of the snow cloud.

Figure 14 shows that the grayscale difference at X = 2.8 m increased first, followed by those at X = 6 m and X = 11.3 m. This progression reflects the process by which snow particles were initially entrained beneath the rotor by the downwash flow and subsequently transported outward as the snow cloud expanded. As shown in Figures 14 and 15, the grayscale differences at all six observation points in Test T03 are consistently greater than those in Test T02, with an average difference of approximately 19.7. This finding is consistent with the snow cloud area analysis presented in the previous section and indicates that the overall snow cloud concentration in Test T03 was significantly higher than that in Test T02. The higher snow concentration in Test T03 compared with T02 is mainly associated with the increased rotor loading under a larger collective pitch angle. A higher collective pitch produces stronger rotor-induced flow and enhanced momentum transfer to the snow surface, thereby increasing snow particle entrainment and transport capability. Consequently, a larger amount of suspended snow particles contributes to the increased local concentration. Furthermore, in Test T02, the grayscale differences measured at 0.3 m were consistently higher than those measured at 1.5 m, indicating that the snow cloud concentration below the rotor disk exceeded that above the rotor disk, consistent with the observations obtained for Test T03. However, unlike Test T03, Test T02 exhibited a distinct spatial distribution pattern in which the snow cloud concentration increased as the observation location approached the rotor axis.

The temporal evolution of ROI1–ROI6 further shows that the grayscale differences in the two tests were relatively similar only during the initial stage of snow particle entrainment. As the experiment progressed, the grayscale differences in Test T02 became increasingly lower than those in Test T03. In particular, at ROI3 and ROI5, located 11.3 m from the rotor axis, the grayscale differences in Test T02 generally remained below 10,

indicating that under the lower collective pitch setting, the snow cloud exhibited limited propagation to distances of 11.3 m from the rotor center.

### *4.4. Snow Particle Flow Structures and Entrainment Mechanisms*

To investigate the flow structures and snow particle entrainment mechanisms induced by rotor downwash, a planar laser qualitative flow visualization experiment was conducted under hovering conditions in Test T04. The corresponding test conditions are listed in Table 3. A continuous-wave laser source was installed on the right side of the helicopter to generate a laser sheet perpendicular to the ground surface. A Canon EOS 90D camera was positioned behind and to the side of the helicopter, with its optical axis oriented perpendicular to the laser sheet plane. The measurement field of view was 4.6 m × 2.5 m, and images were recorded at a frame rate of 25 fps. A schematic diagram of the measurement setup is shown in Figure 16.

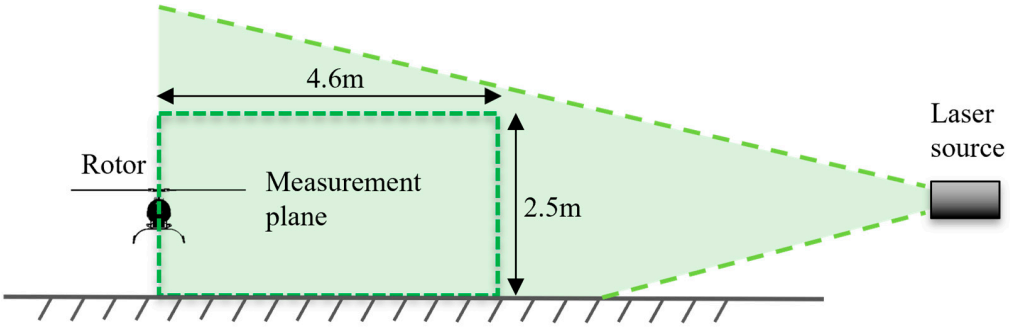



**Figure 16.** Schematic diagram of the snow particle flow visualization measurement system.

The recorded video data were subsequently processed, and a sequence of representative images exhibiting clear snow particle scattering signals and high signal-to-noise ratios was selected, as shown in Figure 17. The image sequence illustrates the typical process by which surface snow particles are transported radially outward and subsequently lifted upward under the influence of rotor tip vortices. Figure 18 presents the propagation trajectory of the rotor-induced vortex and the corresponding snow particle entrainment directions, while Figure 19 shows the evolution of vortex height and horizontal propagation distance.

As illustrated in the figures, the snow particle transport and entrainment process can be divided into four stages.

(a) Initiation of Surface Snow Particles:

When the rotor downwash impinges on the ground surface, a high-speed radial wall jet is generated and propagates outward along the ground. The surface snow layer is subjected to substantial aerodynamic shear stress. Once the local airflow velocity exceeds the critical threshold for particle entrainment, snow particles are detached from the surface and subsequently undergo rolling, saltation, and suspension.

(b) Snow Particle Capture by Rotor Tip Vortices:

As the flow develops, the low-pressure vortex cores and rotational velocity fields associated with the rotor tip vortices appear to become the primary factors governing snow particle motion. Snow particles transported outward by the radial wall jet are progressively captured by the vortex structures. Under the combined effects of upward induced velocity, tangential rotational velocity, and particle inertia, particle trajectories transition from near-ground horizontal transport to curved ascending motion.

(c) Snow Cloud Roll-Up and Recirculation:

As the interaction between the rotor tip vortices and the radial wall jet intensifies, a coherent recirculating vortex structure is observed. This rotating vortex core continuously entrains newly mobilized snow particles while simultaneously recapturing suspended particles that would otherwise dissipate. These particles are reintroduced into the primary flow field and transported to higher elevations.

Under the influence of vortex-induced upwash, the leading edge of the snow cloud is lifted again, producing roll-up and recirculation motions near the upper boundary of the cloud. As a result, both snow cloud height and particle concentration increase rapidly. This stage is considered the primary development phase of the whiteout phenomenon.

(d) Vortex Breakdown and Dispersion:

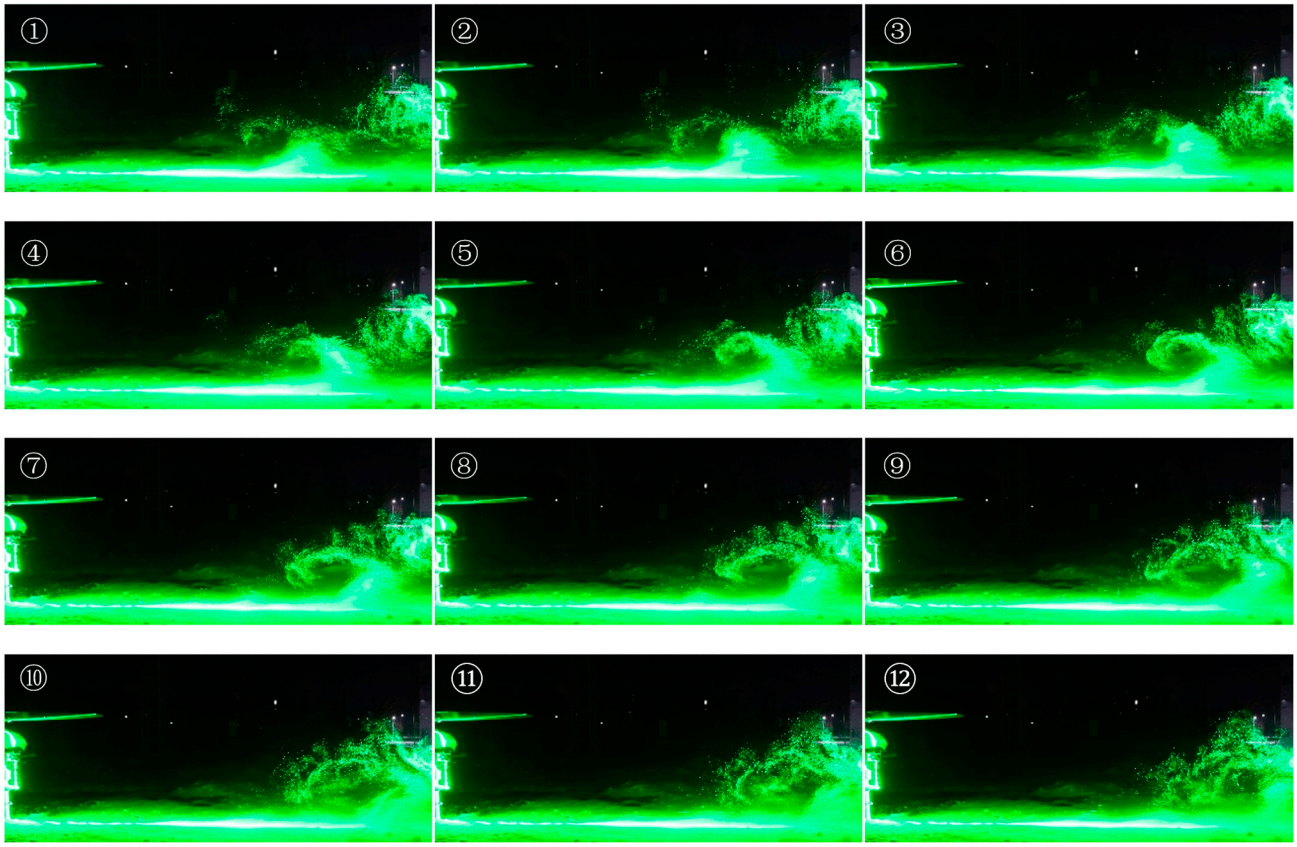



**Figure 17.** Representative time-series images of snow particle motion: Images ①–⑫ show consecutive frames acquired at 25 fps.

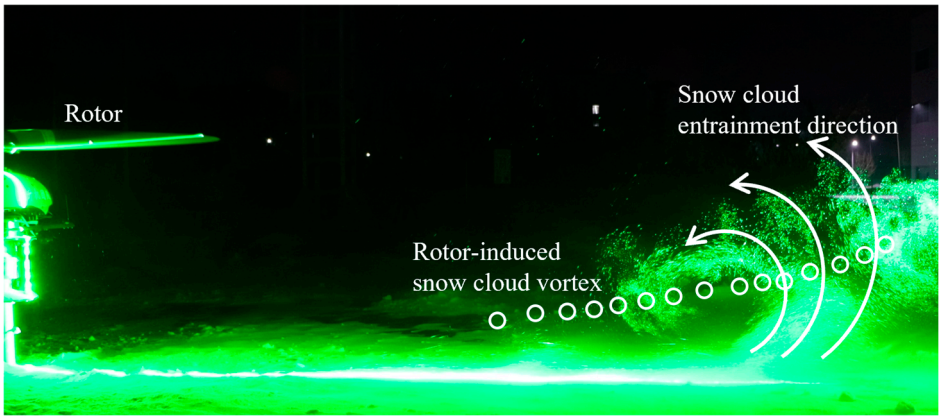



**Figure 18.** Snow particle entrainment process.

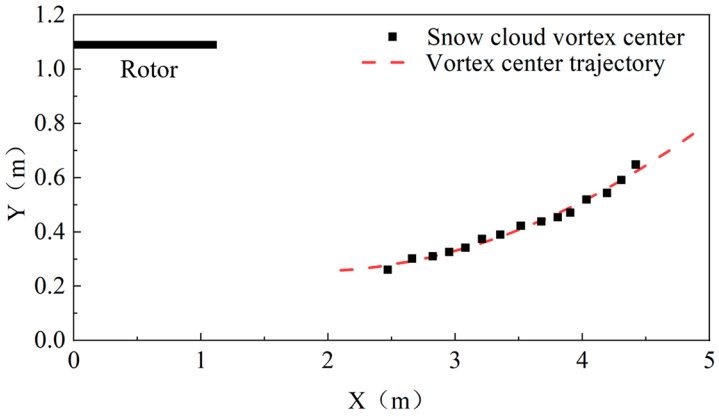



**Figure 19.** Evolution of snow cloud vortex trajectory.

As the vortex structure propagates outward, its stability gradually decreases, eventually leading to vortex breakdown and dissipation. During this stage, snow particles are dispersed over a wider region through the combined effects of turbulent diffusion and recirculating flow structures. In the recorded images, this process appears as a dense snow particle cloud extending across the forward region of the helicopter. Consequently, visual obscuration increases significantly, ultimately resulting in a severe whiteout condition.

## 5. Conclusions

Field experiments involving takeoff, landing, and hovering operations were conducted using an unmanned helicopter with a rotor diameter of 2.2 m under natural low-temperature winter conditions in Harbin. The evolution characteristics and formation mechanisms of rotor-induced snow clouds during near-ground operations over snow-covered surfaces were investigated. The main conclusions are as follows:

(a) During near-ground flight over snow-covered terrain, the rotor-induced downwash is considered a dominant influencing factor affecting snow cloud formation and evolution under the present experimental conditions. The development of the snow cloud was strongly dependent on helicopter altitude and downwash intensity. During takeoff and landing, the proximity of the rotor to the ground enhanced snow particle entrainment, resulting in larger snow cloud areas. Increasing collective pitch leads to an observable increase in snow cloud extent and particle concentration, which is attributed to the enhanced rotor-induced flow and particle entrainment capability.

(b) Rotor-induced snow clouds exhibited a coupled transport process involving particle entrainment, suspension, recirculation, and deposition rather than simple transient dispersion. During hovering, continuous snow particle entrainment and re-entrainment by the rotor-induced flow field produced a persistent recirculating flow structure, allowing elevated snow cloud concentrations to be maintained for extended periods. In addition, the snow cloud concentration exhibited a pronounced non-uniform spatial distribution.

(c) Planar laser qualitative flow visualization revealed the key mechanisms governing snow particle transport and snow cloud evolution. Rotor downwash first generated a high-speed radial wall jet that mobilized surface snow particles through aerodynamic shear. Subsequently, rotor tip vortices captured and transported snow particles upward, transforming their trajectories from near-ground horizontal motion to ascending transport. The recirculation and repeated lifting of suspended particles further increased snow cloud height and concentration. As the vortex structures propagated outward and gradually dissipated, snow particles dispersed over a wider region

through the combined effects of turbulent diffusion and recirculating flow, thereby promoting the development of dense snow cloud regions and reduced visibility.

It should be noted that the present conclusions are based on a limited number of outdoor experiments, and repeated tests under strictly identical conditions were not performed because of the constraints of natural snowfall and field testing. Formal uncertainty estimates for the extracted snow cloud area, spreading distance, and grayscale-difference measurements were also not available. Therefore, the effects of collective pitch and rotor height reported in this study should be regarded as experimentally observed trends under the present test conditions and should not be generalized beyond the tested operating and environmental ranges. Further repeated experiments under controlled conditions are required to establish the statistical repeatability and quantitative uncertainty of these relationships.

**Author Contributions:** Conceptualization, T.S. and W.Y.; methodology, T.S. and X.L.; software, W.Y.; validation, T.S., W.Y. and S.L.; formal analysis, W.Y.; investigation, Z.Y. and X.L.; data curation, S.L.; writing—original draft preparation, W.Y.; writing—review and editing, T.S. and Y.L.; visualization, Z.Y.; supervision, T.S.; project administration, W.Y.; funding acquisition, T.S. All authors have read and agreed to the published version of the manuscript.

**Funding:** This research was funded by the Aeronautical Science Fund of China (2024M058027001).

**Data Availability Statement:** The original contributions presented in this study are included in the article. Further inquiries can be directed to the corresponding author(s).

**Conflicts of Interest:** The authors declare no conflicts of interest.

## References

1. Harker, G.S. Whiteout—A bibliographical survey. *Bull. Am. Meteorol. Soc.* **1959**, *40*, 225–229. [CrossRef]
2. Jennings, S.A. Rotary wing brown-out symbology: The DVEST test. In *Head-and Helmet-Mounted Displays XVII; and Display Technologies and Applications for Defense, Security, and Avionics VI*; SPIE: Bellingham, WA, USA, 2012; Volume 8383, pp. 129–136.
3. Perrotta, G.M. Characterization of Rotor Wake in Ground Effect. In Proceedings of the 53rd AIAA Aerospace Sciences Meeting, Kissimmee, FL, USA, 5–9 January 2015; p. 0370.
4. Brown, R.E.; Whitehouse, G.R. Modelling rotor wakes in ground effect. *J. Am. Helicopter Soc.* **2004**, *49*, 238–249. [CrossRef]
5. Brown, R.E.; Line, A.J. Efficient high-resolution wake modeling using the vorticity transport equation. *AIAA J.* **2005**, *43*, 1434–1443. [CrossRef]
6. Lee, T.E.; Leishman, J.G.; Ramasamy, M. Fluid dynamics of interacting blade tip vortices with a ground plane. *J. Am. Helicopter Soc.* **2010**, *55*, 22005. [CrossRef]
7. Sydney, A.; Leishman, J.G. Measurements of Rotor/Airframe Interactions in Ground Effect Over a Sediment Bed. In Proceedings of the 69th Annual Forum of the American Helicopter Society, Phoenix, AZ, USA, 21–23 May 2013.
8. Sydney, A.; Leishman, J.G. Time-resolved measurements of rotor-induced particle flows produced by a hovering rotor. *J. Am. Helicopter Soc.* **2014**, *59*, 1–16. [CrossRef]
9. Zhu, M.; Zhao, Q.; Wang, B. Simulation of helicopter rotor in ground effect based on CFD method and hybrid trim algorithm. *Acta Aeronaut. Astronaut. Sin.* **2016**, *37*, 2539–2551.
10. Pasquali, C.; Serafini, J.; Bernardini, G.; Milluzzo, J.; Gennaretti, M. Numerical-experimental correlation of hovering rotor aerodynamics in ground effect. *Aerosp. Sci. Technol.* **2020**, *106*, 106079. [CrossRef]
11. Phillips, C.; Brown, R.E. Eulerian simulation of the fluid dynamics of helicopter brown-out. *J. Aircr.* **2009**, *46*, 1416–1429. [CrossRef]
12. Phillips, C.; Kim, H.W.; Brown, R.E. The flow physics of helicopter brownout. In Proceedings of the 66th American Helicopter Society Forum: Rising to New Heights in Vertical Lift Technology, Phoenix, AZ, USA, 11–13 May 2010.
13. Jasion, G. Toward a Physics Based Entrainment Model for Simulation of Helicopter Brownout. Ph.D. Thesis, University of Southampton, Southampton, UK, 2013.
14. Porcù, R.; Miglio, E.; Parolini, N.; Penati, M.; Vergopolan, N. HPC simulations of brownout: A noninteracting particles dynamic model. *Int. J. High Perform. Comput. Appl.* **2020**, *34*, 267–281. [CrossRef]
15. Cao, Y.; Wang, G.; Jiang, C. Study on influencing factors of helicopter brownout evolution based on CFD-DEM. *Appl. Sci.* **2021**, *12*, 126. [CrossRef]

16. Tanner, P.E. Photogrammetric characterization of a brownout cloud. In Proceedings of the American Helicopter Society International 67th Annual Forum and Technology Display, Beach, VA, USA, 3–5 May 2011; p. NF1676L-11463.
17. Wong, O.D.; Tanner, P.E. Photogrammetric measurements of an EH-60L brownout cloud. *J. Am. Helicopter Soc.* **2016**, *61*, 1–10. [CrossRef]
18. Raffel, M.; Kindler, K.; Mulleners, K.; Heineck, J. Particle Image Velocimetry in Helicopter Aerodynamics: Developments, Challenges, and Trends. In *American Helicopter Society 68th Annual Forum*; Curran Associates, Inc.: Red Hook, NY, USA, 2012; Volume 9.
19. Valance, A.; Rasmussen, K.R.; El Moctar, A.O.; Dupont, P. The physics of aeolian sand transport. *Comptes Rendus Phys.* **2015**, *16*, 105–117. [CrossRef]
20. Li, J.; Guala, M.; Hong, J. Snow particle analyzer for simultaneous measurements of snow density and morphology. *J. Geophys. Res. Atmos.* **2023**, *128*, e2023JD038987. [CrossRef]
21. Ebersole, J.F. Obscuration by helicopter-produced snow clouds. *Opt. Eng.* **1983**, *22*, 94–99. [CrossRef]
22. Zhou, X.; Li, X.; Gu, M.; Zhang, Y. Two-equation model for numerical simulation on snow drifting. *Acta Aerodyn. Sin.* **2012**, *30*, 640–645.
23. Matsuzawa, M.; Takeuchi, M. Study on Methods to Calculate Visibility on Blowing Snow. In Proceedings of the 11th International Road Weather Conference, Standing International Road Weather Commission, Sapporo, Japan, 26–28 January 2002.
24. Ryerson, C.; Haehnel, R.; Koenig, G.; Moulton, M. Visibility enhancement in rotorwash clouds. In Proceedings of the 43rd AIAA Aerospace Sciences Meeting and Exhibit, Reno, NV, USA, 10–13 January 2005; p. 263.
25. Treaty, N.A. *Rotary-Wing Brownout Mitigation: Technologies and Training*; North Atlantic Treaty Organization: Brussels, Belgium, 2012.
26. Viertler, F.; Hajek, M. Evaluation of visual augmentation methods for rotorcraft pilots in degraded visual environments. *J. Am. Helicopter Soc.* **2017**, *62*, 1–11. [CrossRef]
27. Montalban, K. Advancing LiDAR Perception in Degraded Visual Environments: A Probabilistic Approach for Degradation Analysis and in Inference of Visibility. Ph.D. Thesis, ISAE Université de Toulouse, Toulouse, France, 2023.
28. Warren, S.G. Optical properties of ice and snow. *Philos. Trans. R. Soc. A Math. Phys. Eng. Sci.* **2019**, *377*, 20180161. [CrossRef] [PubMed]
29. Nathan, N.D.; Green, R.B. Flow visualisation of the helicopter brown-out phenomenon. *Aeronaut. J.* **2009**, *113*, 467–478. [CrossRef]
30. Ishimoto, H.; Adachi, S.; Yamaguchi, S.; Tanikawa, T.; Aoki, T.; Masuda, K. Snow particles extracted from X-ray computed microtomography imagery and their single-scattering properties. *J. Quant. Spectrosc. Radiat. Transf.* **2018**, *209*, 113–128. [CrossRef]
31. Ingvander, S.; Brown, I.A.; Jansson, P.; Holmlund, P.; Johansson, C.; Rosqvist, G. Particle size sampling and object-oriented image analysis for field investigations of snow particle size, shape, and distribution. *Arct. Antarct. Alp. Res.* **2013**, *45*, 330–341. [CrossRef]
32. Serra, J. *Image Analysis and Mathematical Morphology*; Academic Press, Inc.: Cambridge, MA, USA, 1983.
33. Gonzalez, R.C.; Woods, R.E. *Digital Image Processing*; Prentice Hall: Upper Saddle River, NJ, USA, 2002.
34. Canny, J. A computational approach to edge detection. *IEEE Trans. Pattern Anal. Mach. Intell.* **1986**, *6*, 679–698. [CrossRef]

**Disclaimer/Publisher's Note:** The statements, opinions and data contained in all publications are solely those of the individual author(s) and contributor(s) and not of MDPI and/or the editor(s). MDPI and/or the editor(s) disclaim responsibility for any injury to people or property resulting from any ideas, methods, instructions or products referred to in the content.